

pubs.acs.org/journal/apchd5 Letter

Large-Area Ultrathin Moiré Chiral Metamaterials by Thermal-Tape-Transfer Printing

Anand Swain, Zhihan Chen, Yaoran Liu, Zilong Wu, and Yuebing Zheng*



Cite This: ACS Photonics 2023, 10, 1225-1231



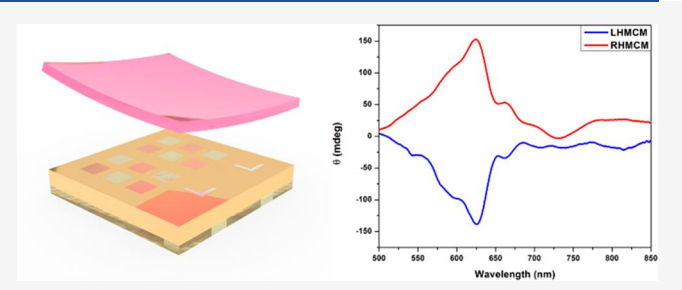
ACCESS

Metrics & More

Article Recommendations

Supporting Information

ABSTRACT: Moiré chiral metamaterials (MCMs) consisting of stacked plasmonic nanohole arrays with twist angles exhibit strong chiroptical response, thereby opening doors to ultrathin chiroptical sensors, switches, and detectors. The existing fabrication of MCMs on the basis of colloidal lithography results in significant inhomogeneity within the structure, which impairs the responsiveness and tunability of its optical chirality. Here, we develop thermal-tape-transfer printing to enable the fabrication of large-scale and homogeneous MCMs with arbitrary twist angles and tunable optical chirality. As a demonstration, large-scale (100 \times



 $100 \ \mu m^2$) gold MCMs with an ultrathin thickness ($\sim 40 \ nm$) were fabricated, which marked a 10-fold increase in single domain size over the colloidal lithographic method, while showing spatially uniform and strong chiroptical response. With the ultrathin thickness and high tunability, the MCMs developed by our fabrication method will advance a variety of biological, photonic, and optoelectronic applications.

KEYWORDS: Moiré chiral metamaterials, thermal-tape-transfer printing, chiroptical response

hirality describes the property of nonsuperimposable mirror symmetry. Optical chirality has been demonstrated as an effective route to manipulate excitons and has been used in the search for extraterrestrial life. It is also instrumental in chemical synthesis, inaging, and drug pharmacokinetics. Since optical chirality is typically difficult to measure because of the weak chiral response of natural materials, chiral metamaterials, which are artificial subwavelength structures with strong chiroptical responses, have been used to overcome these limitations. Chiral metamaterials can be broadly classified into inherently chiral structures (intrinsic chirality) and strategically stacked achiral structures (extrinsic chirality) and have been exploited in applications such as superconductivity, biosensing, metamirrors, and detectors. Since of notice o

Moiré chiral metamaterials (MCMs) are a prominent example of stacked planar chiral structures, ^{16,21,30} which derive their chiral character from an in-plane rotation between two or more stacked layers where the twist angle controls the chiroptical response of the structures. Recent demonstrations of MCMs have shown the immense potential of these metamaterials in many applications, such as reconfigurable light absorbers, ³¹ dynamic beamforming, ³² chiral detectors, ³³ and surface-enhanced Raman spectroscopy (SERS). ³⁴ Single-domain MCMs afford uniform chiral regions and consequently offer controllable and scalable structures for applications in metabolite detection ³⁰ and optoelectronic devices. ³⁵ Current strategies to fabricate MCMs mostly rely on lithographic methods, which are challenging in producing the MCMs with

the uniformity over the larger areas and precise control over the twist angle for their effective applications in optoelectronics and biology.³⁶ Specifically, lithographic methods, such as electron-beam lithography and focused-ion-beam lithography, can fabricate MCMs with precise in-plane rotation and longrange order and uniformity.³⁷ However, these methods often involve complex steps with a need for precise mask alignment, which drives up costs and reduces throughput. 16,38,39 Conversely, colloidal assembly methods like Moiré nanosphere lithography allow for the cost-effective construction of MCMs⁴⁰ with multiple domains of little control over the twist angle, which impedes high-throughput chiral detection 40 and large-scale optoelectronics.³² As a result, current fabrication methods for MCMs suffer from limitations in throughput and are unable to successfully achieve singledomain nanostructures over large areas controllably. 30,41

Herein, we have developed a thermal-tape-transfer printing method for the fabrication of MCMs with a single domain and tunable twist angles over large scale (>100 \times 100 μm^2). Transfer printing is a promising method to fabricate MCMs with large-scale uniformity and high throughput while being

Received: February 17, 2023 Published: May 4, 2023





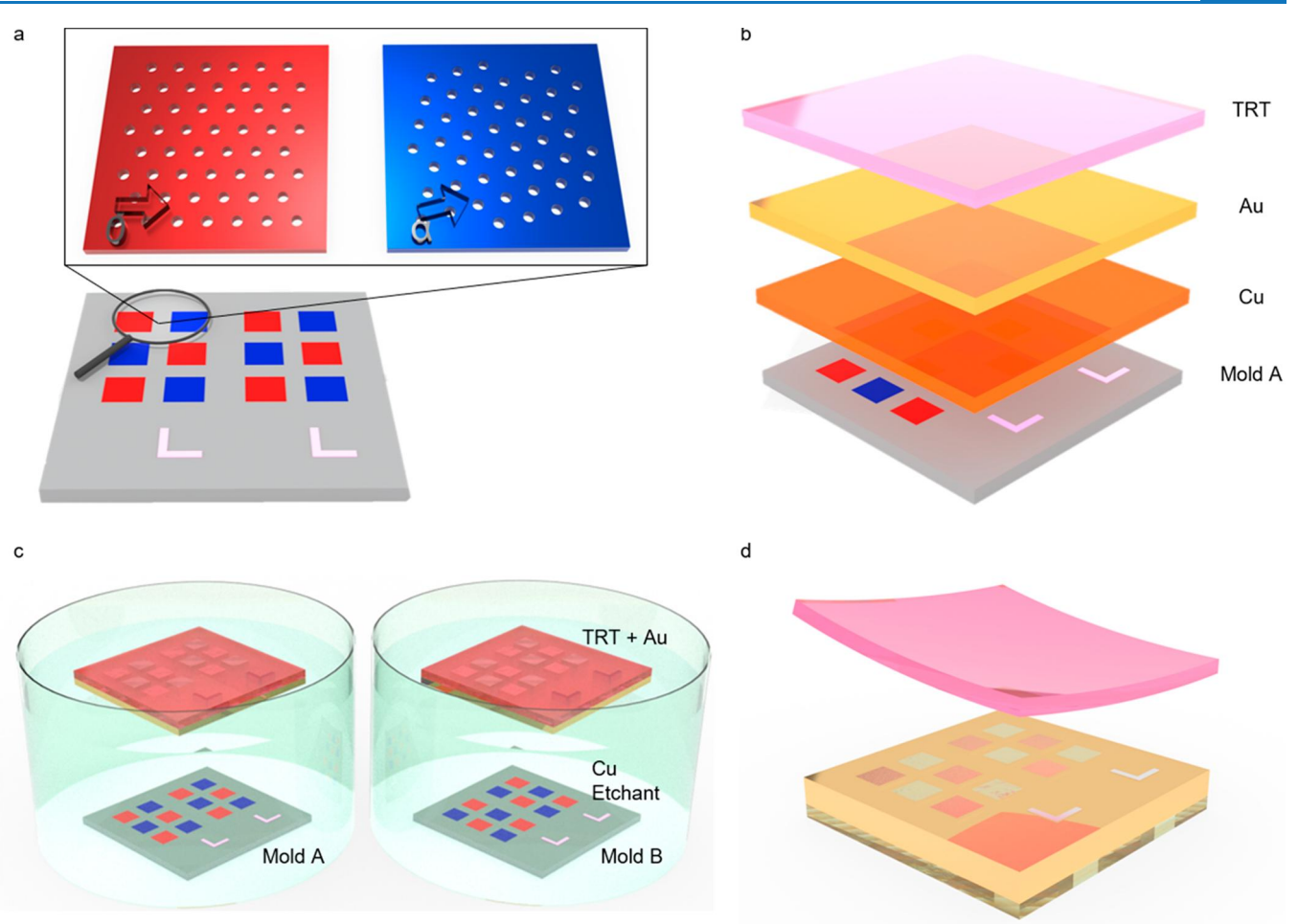


Figure 1. Fabrication of Au MCMs on the basis of thermal tape transfer printing. (a) The individual nanohole regions with alternate 0° (red) and α (blue) regions. $\alpha \in [0^{\circ},60^{\circ}]$ for hexagonal nanohole arrays. (b) Cu followed by Au were deposited on the mold by e-beam physical vapor deposition, and the TRT was applied on top. (c) The mold separates from the TRT-Au layer by etching out the Cu layer. The process is repeated with Mold B to yield the complementary regions for the second layer. (d) Stacking assembly is executed by transferring the first layer on the glass substrate, followed by transfer of the second layer on top.

less complex and relatively inexpensive. 42,43 Briefly, a patterned mold is first coated by the material of choice through various deposition techniques, which is then transferred to a substrate via differential adhesion among the mold, a transferring layer [e.g., poly(methyl methacrylate) (PMMA),^{44,45} polydimethylsiloxane (PDMS)^{46–48} layers, and thermal release tapes (TRTs)^{49,50}), and the substrate through either dry⁴⁸ or wet⁵¹ processing. In this work, we make use of a lowtemperature TRT dry release technique. Compared with prevalent fabrication methods, such as nanosphere lithography, that have limited MCM domains ($\sim 30 \times 30 \ \mu m^2$) and uncontrollable twist angles,³⁰ the patterned molds ensure the structural uniformity of each layer of MCMs while the use of the transfer tape leads to the precise control of the twist angle. Additionally, the dry-release process and ambient-temperature operations avoid residual solvent molecules and potential thermal distortion of the structure, which enhances the chiroptical detection accuracy of the MCMs. Moreover, the simultaneous fabrication of complementary MCM enantiomeric structures on one device is targeted to streamline the detection method for chiral metabolites.

The fabrication process mainly consists of three procedures, including mold fabrication, material deposition, and two-step transferring and stacking. As the Au MCMs are composed of

two Au nanohole arrays with twisted angles, we first fabricated hexagonal nanohole array molds through e-beam lithography. Two molds were fabricated with alternating 0° and α regions (Figure 1a). Vertical stacking of a 0° region on top of an α region leads to a left-handed (LH) enantiomeric MCM region, and the opposite stacking leads to a right-handed (RH) region. Mold A and Mold B were two molds fabricated as inverses in their layouts, which enabled the fabrication of multiple different MCM domains on one set of molds, simultaneously. Moreover, complementary MCMs can be easily obtained by reusing the molds in reverse sequence (i.e., mold A stacked on mold B versus mold B stacked on mold A). Note that a copper (Cu) layer was deposited before the Au deposition, which serves as a sacrificial layer for the following transfer process.

Postdeposition, the TRT was applied to the surface of the Au nanohole arrays (Figure 1b). The mold with the TRT was then put on the surface of the Cu etchant solution for 4 h until the mold sank to the bottom, and the Au layer with the TRT floated on the solution (Figure 1c). We chose Cu as our sacrificial layer because the Cu etchant does not significantly react with the Au film, thereby ensuring clean separation. To get rid of traces of etchant, the Au layer, along with the TRT, was cleaned twice by immersion in DI water. The TRT was trimmed along three edges, by which fine cracks were

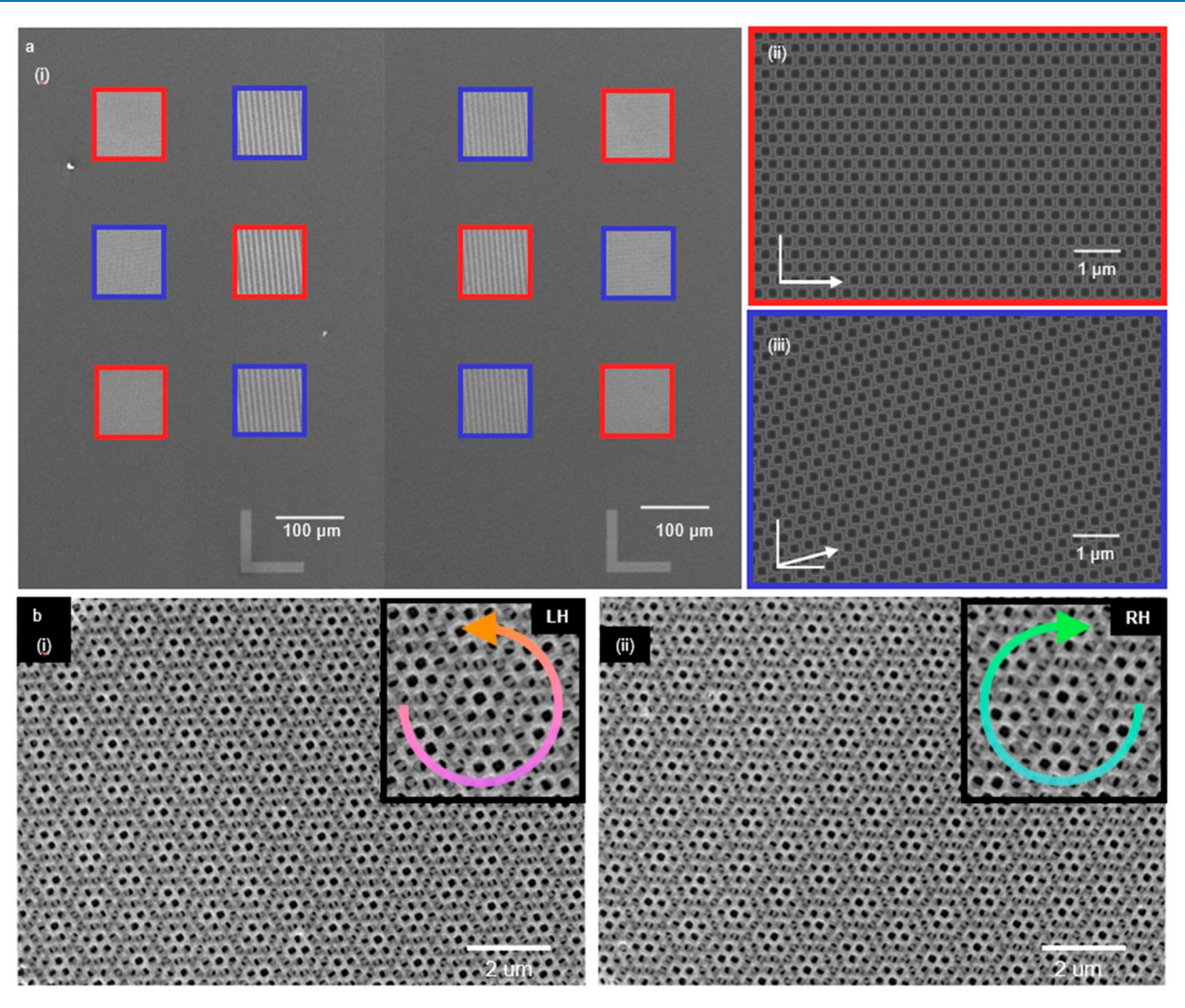


Figure 2. SEM images of the molds and MCMs. (a) (i) SEM images of mold A (left) and B (right) with the alternatively arranged nanohole patterns. Magnified images of (ii) the 0° angle arrays and (iii) 15° angle arrays. The L-shaped alignment marks are placed below the nanohole regions for precise alignment. (b) SEM images of (i) LH Au MCMs and (ii) RH Au MCMs. Magnified images of the MCM structures are inset at the top-right corners.

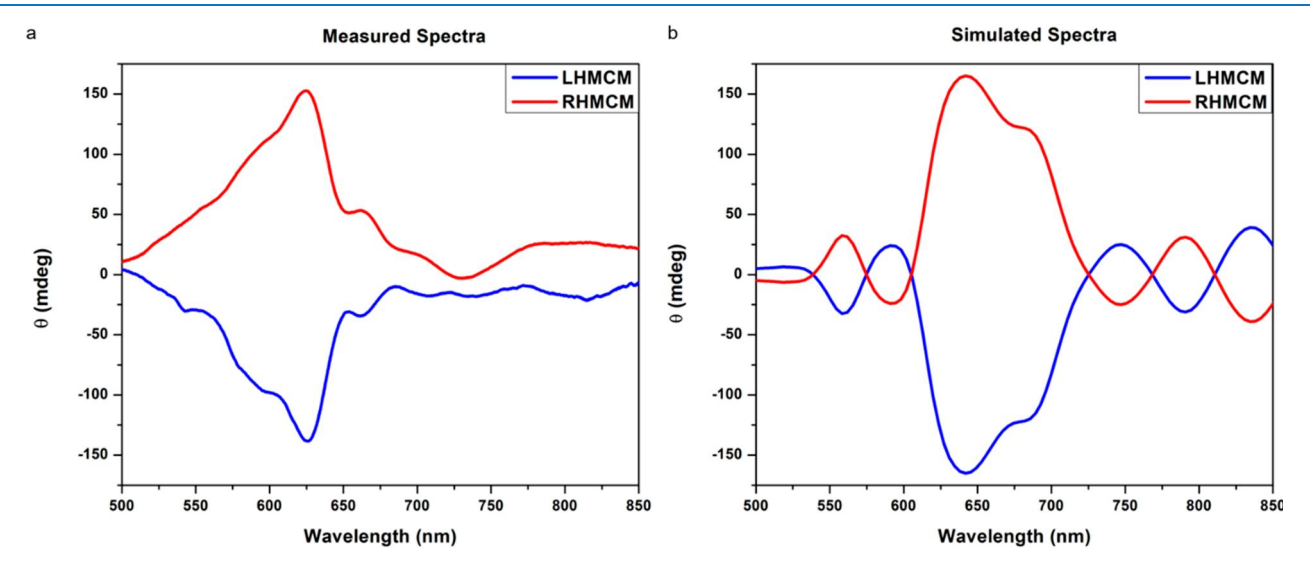


Figure 3. Optical characterization of 15° Au MCMs. (a) Experimental ellipticity spectra. The prominent peak with different signs is shown around 625 nm for MCMs with opposite handedness. (b) Simulated ellipticity spectra where the major peak exists around 640 nm.

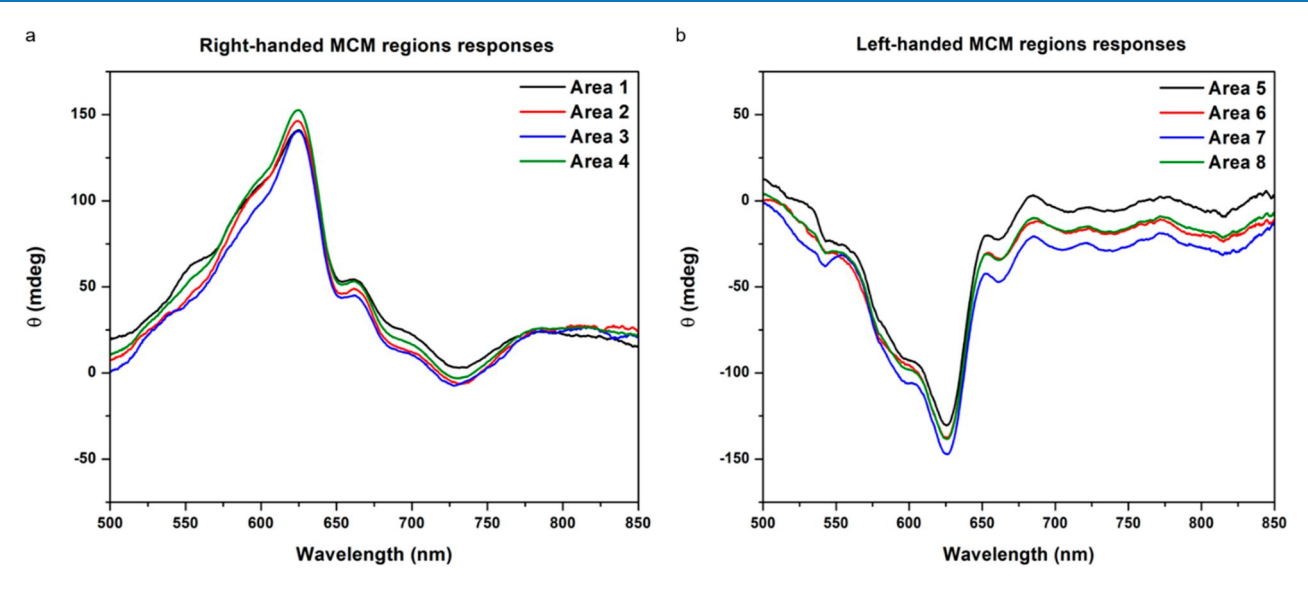


Figure 4. Optical characterization of discrete Au MCM regions. (a) Ellipticity spectra for right-handed MCM regions. (b) Ellipticity spectra for left-handed MCM regions. Minimal peak shift is observed in the major peak at 625 nm with a slight change in minor peak positions.

introduced in the Au film to provide channels for the total drainage of potential trapped water in the nanohole region. Thereafter, the tape was gently placed on a clean borosilicate glass substrate. The cleaning procedure of the substrate resulted in a hydrophilic substrate, which enhanced the adhesion strength between the substrate and the Au film. Finally, the substrate with the TRT was completely dried by being placed at an incline in a vacuum chamber at room temperature and around $-100~\rm kPa$ gauge pressure for 5 days. To peel off the TRT, the substrate was first preheated for 4 h on a thermal plate at 60 °C and, then, raised to 110 °C for the total removal of the tape.

After the peel-off transfer of the first layer based on mold A, the TRT with Au from mold B was processed by the same procedures mentioned above and finally stacked on top of the first layer. The alignment markers were used to make sure both layers were aligned at the desired angle under an optical microscope at 10× magnification. After stacking, the substrate with the two Au layers was placed in the vacuum chamber again for complete drying.

By using our thermal release transfer printing technique, we have fabricated thin and large-scale uniform Au MCMs as effective chiroptical devices (Figure 2b). We chose α to be 15° because it has previously shown a stronger chiroptical response. The scanning electron microscope (SEM) images of molds A and B are shown in Figure 2a with the alternative regions at 0° (red) and 15° (blue). Each individual nanohole domain was 100 × 100 μ m². Since Molds A and B are exact inverses in layout, 12 MCMs were obtained by overlapping these two layers, which are divided into two enantiomeric structures, i.e., left handed (LH) MCMs [Figure 2b(i)] and right handed (RH) MCMs [Figure 2b(ii)].

The fabricated Au MCMs were optically characterized to measure their chiroptical properties and also to evaluate the quality of the fabrication. To quantify the circular dichroism (CD) of the structures, ellipticity (θ) is used as

$$\theta = \tan^{-1} \frac{(\sqrt{T_{\text{LCP}}} - \sqrt{T_{\text{RCP}}})}{(\sqrt{T_{\text{LCP}}} + \sqrt{T_{\text{RCP}}})}$$

where $T_{\rm LCP}$ and $T_{\rm RCP}$ are the optical transmissions under LCP and RCP light, respectively. 19 Figure 3a shows the ellipticity obtained experimentally, which matches well with the simulated results in Figure 3b. The spectra show a good match in the major peaks, where the peak shift can be attributed to the slight shape variation of nanoholes and the difference of the Au refractive index between the deposited Au and what is used in simulations.⁵³ Furthermore, our structures have a strong optical response, i.e., a sharp θ value of ~150 mdeg at the peak wavelength, with the structure's thickness only being ~40 nm. This strong response is attributed to the close contact of the conductive individual layers, which leads to strong light-matter interaction and light-driven surface currents. Moreover, the conductive contact makes our structure compatible for use in optoelectronic applications, as well.54

In order to demonstrate the uniformity of our fabricated structures, we characterized the chiroptical responses of four regions in a single right-handed (Figure 4a) and four regions in a left-handed MCM domain (Figure 4b). SEM images of the regions are shown in Supplementary Figure S1. We observed that the major peaks were consistent in their positions with a minimal variation in the minor peaks. Further, there was a small variation in the relative intensities of the individual peaks, which could be attributed to the local fabrication defects. We successfully concluded that the fabricated structures are uniform in the MCM domains.

In summary, we have demonstrated a versatile thin film transfer technique on the basis of thermal release tape for the fabrication of MCMs with tunable rotational angles and chiroptical response. Au MCMs with a thickness of 40 nm and single domain over $100 \times 100~\mu\text{m}^2$ were fabricated with demonstrated strong CD signals (~150 mdeg). The simultaneous fabrication of complementary MCM enantiomeric structures on one device can facilitate fast enantiodiscrimination in biological studies by eliminating the need to search for complementary detection domains, as has been the case in MCMs manufactured through colloidal assembly methods. This also promises to make point-of-care chiral detection feasible. Moreover, our technique is compatible with the fabrication of most stacked materials and is effective in

the low-cost scale-up of previous fabrication techniques (e.g., pure e-beam lithography, colloidal assembly). Specifically, we have used physical vapor deposition to deposit individual layers in our method, which is also used for the current fabrication methods in 2D materials. Further, our molds are also reusable because they were reused for 150 cycles with a simple piranha solution cleaning with no damage and with no effect on the transferred layers. In addition to this, the scope of our method can also extend to flexible substrates, as transfer printing has been shown to be effective in the fabrication of flexible electronics. S6-58

MATERIALS AND METHODS

Silicon hexagonal nanohole array molds were fabricated through electron-beam (e-beam) lithography (Elionix ELS-G100) at a dose of 600 μ C/cm², shot pitch of 10 nm, and a current of 2 nA. To have a chiroptical response within the visible spectrum, the nanoholes were designed to be 230 nm in diameter with a depth of 100 nm and a lattice parameter of 300 nm. A PMMA mask layer was used, and reactive ion etching (RIE180, Oxford Instruments) was implemented. SF₆ at 100 sccm was used with an rf power of 25 W and an ICP power of 100 W with helium cooling. For precise alignment, L-shaped alignment markers were included in the mold to serve as a guide for controlled stacking. Au and Cu deposition were carried out in an e-beam evaporation unit (PVD75, Kurt J Leskar Company). Cu etching was carried out in an APS-100 from Transene Inc. DI water was used for all washing steps. The TRT (REVALPHA) used was obtained from Nitto Denko Corporation. Glass substrates were cleaned for 1 min in a freshly prepared piranha solution and subsequently treated with oxygen plasma for 15 min. Stacking of the layers was carried out under an optical microscope (Leica DMi1) at 10× magnification. Poststacking drying was carried out in a vacuum chamber (VWR International).

To probe the optical response of the Au MCMs, the transmission spectra were measured using an inverted microscope (Ti-E, Nikon Inc.) integrated with a spectrometer (Shamrock 303i, Andor). A halogen lamp (Nikon Inc., 12 V, 100 W) was used as the light source. The circularly polarized light was obtained by subsequently passing the incident light through a linear polarizer (LPNIRE100-B, Thorlabs Inc.) and a quarter-wave plate (AQWP10M-980, Thorlabs Inc.). The fast axis of the quarter-wave plate was rotated with respect to the linear polarizer to switch between the left circularly polarized (LCP) or right circularly polarized (RCP) light. Afterward, the circularly polarized light passed through the center of each domain, and the transmitted parts were collected by the objective (Nikon Inc., 40X). A slit with a tunable width (50 to 2500 μ m) was placed between the objective and the spectrometer. Areas of 500 μ m² were chosen to measure the optical response of the MCMs as a whole.

To verify the experimental results, we further simulated the chiroptical spectra for the Au MCMs using the finite-difference time-domain (FDTD) method (Lumerical, ANSYS). An LCP or RCP light was irradiated onto the top of the MCMs on a glass substrate. The refractive index of the glass substrate was set as 1.46. The optical constants of the Au were obtained from Johnson and Christy. The thickness of each Au layer was set as 20 nm, with the coarse mesh being 5 nm for the background and a fine mesh of 2.5 nm at the gold—gold contact.

ASSOCIATED CONTENT

Supporting Information

The Supporting Information is available free of charge at https://pubs.acs.org/doi/10.1021/acsphotonics.3c00222.

SEM images of the left- and right-handed MCM regions characterized corresponding to the regions depicted in Figure 4 (PDF)

AUTHOR INFORMATION

Corresponding Author

Yuebing Zheng — Texas Materials Institute and Department of Electrical and Computer Engineering, The University of Texas at Austin, Austin, Texas 78712, United States; orcid.org/0000-0002-9168-9477; Email: zheng@austin.utexas.edu

Authors

Anand Swain — Texas Materials Institute, The University of Texas at Austin, Austin, Texas 78712, United States Zhihan Chen — Texas Materials Institute, The University of Texas at Austin, Austin, Texas 78712, United States Yaoran Liu — Department of Electrical and Computer Engineering, The University of Texas at Austin, Austin, Texas 78712, United States

Zilong Wu – Texas Materials Institute, The University of Texas at Austin, Austin, Texas 78712, United States; orcid.org/0000-0001-9323-7768

Complete contact information is available at: https://pubs.acs.org/10.1021/acsphotonics.3c00222

Author Contributions

Y.Z., Y.L., and Z.W. conceived and designed the experiments. A.S. conducted experiments on the transfer protocol and performed optical measurements and data analysis. Z.C. conducted the optical simulations. Y.Z. supervised the project. All authors were involved in discussing the results and writing the manuscript.

Funding

This work was funded by the National Science Foundation (NSF-ECCS- 2001650) and the National Institutes of Health (R01GM146962).

Notes

The authors declare no competing financial interest.

ACKNOWLEDGMENTS

The authors thank the Texas Advanced Computing Center (TACC) at the University of Texas at Austin for providing high-performance computing resources.

■ REFERENCES

- (1) Kotov, N. A.; Liz-Marzán, L. M.; Weiss, P. S. Chiral Nanostructures: New Twists. ACS Nano 2021, 15 (8), 12457–12460. (2) Capaz, R. B.; Spataru, C. D.; Ismail-Beigi, S.; Louie, S. G. Diameter and chirality dependence of exciton properties in carbon nanotubes. Phys. Rev. B 2006, 74 (12), No. 121401.
- (3) Parnell, J.; Cullen, D.; Sims, M. R.; Bowden, S.; Cockell, C. S.; Court, R.; Ehrenfreund, P.; Gaubert, F.; Grant, W.; Parro, V.; et al. Searching for life on Mars: selection of molecular targets for ESA's Aurora ExoMars mission. *Astrobiology* **2007**, *7* (4), 578–604.
- (4) Naaman, R.; Paltiel, Y.; Waldeck, D. H. Chiral induced spin selectivity gives a new twist on spin-control in chemistry. *Acc. Chem. Res.* **2020**, 53 (11), 2659–2667.

- (5) Evers, F.; Aharony, A.; Bar-Gill, N.; Entin-Wohlman, O.; Hedegård, P.; Hod, O.; Jelinek, P.; Kamieniarz, G.; Lemeshko, M.; Michaeli, K.; et al. Theory of chirality induced spin selectivity: Progress and challenges. *Adv. Mater.* **2022**, *34* (13), 2106629.
- (6) Ben-Moshe, A.; Maoz, B. M.; Govorov, A. O.; Markovich, G. Chirality and chiroptical effects in inorganic nanocrystal systems with plasmon and exciton resonances. *Chem. Soc. Rev.* **2013**, *42* (16), 7028–7041.
- (7) Khorasaninejad, M.; Chen, W.; Zhu, A.; Oh, J.; Devlin, R.; Rousso, D.; Capasso, F. Multispectral chiral imaging with a metalens. *Nano Lett.* **2016**, *16* (7), 4595–4600.
- (8) Kumari Rayala, V. V. S. P.; Kandula, J. S.; P, R. Advances and challenges in the pharmacokinetics and bioanalysis of chiral drugs. *Chirality* **2022**, *34*, 1298–1310.
- (9) Vargesson, N. Thalidomide-induced teratogenesis: History and mechanisms. *Birth Defects Research Part C: Embryo Today: Reviews* **2015**, 105 (2), 140–156.
- (10) Esposito, M.; Tasco, V.; Todisco, F.; Cuscunà, M.; Benedetti, A.; Sanvitto, D.; Passaseo, A. Triple-helical nanowires by tomographic rotatory growth for chiral photonics. *Nat. Commun.* **2015**, *6* (1), 6484.
- (11) Cao, T.; Zhang, L.; Simpson, R. E.; Wei, C.; Cryan, M. J. Strongly tunable circular dichroism in gammadion chiral phase-change metamaterials. *Opt. Express* **2013**, *21* (23), 27841–27851.
- (12) Karimullah, A. S.; Jack, C.; Tullius, R.; Rotello, V. M.; Cooke, G.; Gadegaard, N.; Barron, L. D.; Kadodwala, M. Disposable plasmonics: plastic templated plasmonic metamaterials with tunable chirality. *Adv. Mater.* **2015**, 27 (37), 5610–5616.
- (13) Schnell, M.; Sarriugarte, P.; Neuman, T.; Khanikaev, A.; Shvets, G.; Aizpurua, J.; Hillenbrand, R. Real-space mapping of the chiral near-field distributions in spiral antennas and planar metasurfaces. *Nano Lett.* **2016**, *16* (1), 663–670.
- (14) Dietrich, K.; Lehr, D.; Helgert, C.; Tünnermann, A.; Kley, E. B. Circular dichroism from chiral nanomaterial fabricated by on-edge lithography. *Adv. Mater.* **2012**, *24* (44), OP321–OP325.
- (15) Wang, Z.; Cheng, F.; Winsor, T.; Liu, Y. Optical chiral metamaterials: a review of the fundamentals, fabrication methods and applications. *Nanotechnology* **2016**, *27* (41), 412001.
- (16) Wu, Z.; Zheng, Y. Moiré metamaterials and metasurfaces. Advanced Optical Materials 2018, 6 (3), 1701057.
- (17) Cao, T.; Li, Y.; Wei, C.-W.; Qiu, Y.-m. Numerical study of tunable enhanced chirality in multilayer stack achiral phase-change metamaterials. *Opt. Express* **2017**, *25* (9), 9911–9925.
- (18) Zhou, H.; Xie, T.; Taniguchi, T.; Watanabe, K.; Young, A. F. Superconductivity in rhombohedral trilayer graphene. *Nature* **2021**, 598 (7881), 434–438.
- (19) García-Guirado, J.; Svedendahl, M.; Puigdollers, J.; Quidant, R. Enantiomer-selective molecular sensing using racemic nanoplasmonic arrays. *Nano Lett.* **2018**, *18* (10), 6279–6285.
- (20) Cen, M.; Wang, J.; Liu, J.; He, H.; Li, K.; Cai, W.; Cao, T.; Liu, Y. J. Ultrathin Suspended Chiral Metasurfaces for Enantiodiscrimination. *Adv. Mater.* **2022**, *34*, 2203956.
- (21) Wu, Z.; Chen, X.; Wang, M.; Dong, J.; Zheng, Y. Highperformance ultrathin active chiral metamaterials. *ACS Nano* **2018**, *12* (5), 5030–5041.
- (22) Knipper, R.; Kopecky, V., Jr; Huebner, U.; Popp, J. r.; Mayerhöfer, T. G. Slit-enhanced chiral-and broadband infrared ultrasensing. *ACS Photonics* **2018**, *5* (8), 3238–3245.
- (23) Hendry, E.; Carpy, T.; Johnston, J.; Popland, M.; Mikhaylovskiy, R.; Lapthorn, A.; Kelly, S.; Barron, L.; Gadegaard, N.; Kadodwala, M. Ultrasensitive detection and characterization of biomolecules using superchiral fields. *Nature Nanotechnol.* **2010**, *5* (11), 783–787.
- (24) Niu, C.; Zhao, J.; Du, L.; Liu, N.; Wang, Z.; Huang, W.; Li, X. Spatially dispersive dichroism in bianisotropic metamirrors. *Appl. Phys. Lett.* **2018**. *113* (26), 261102.
- (25) Semnani, B.; Flannery, J.; Al Maruf, R.; Bajcsy, M. Spin-preserving chiral photonic crystal mirror. *Light: Science & Applications* **2020**, 9 (1), 23.

- (26) Wang, Z.; Jia, H.; Yao, K.; Cai, W.; Chen, H.; Liu, Y. Circular dichroism metamirrors with near-perfect extinction. *Acs Photonics* **2016**, 3 (11), 2096–2101.
- (27) Jing, L.; Wang, Z.; Maturi, R.; Zheng, B.; Wang, H.; Yang, Y.; Shen, L.; Hao, R.; Yin, W.; Li, E.; et al. Gradient chiral metamirrors for spin-selective anomalous reflection. *Laser & Photonics Reviews* **2017**, *11* (6), 1700115.
- (28) Li, W.; Coppens, Z. J.; Besteiro, L. V.; Wang, W.; Govorov, A. O.; Valentine, J. Circularly polarized light detection with hot electrons in chiral plasmonic metamaterials. *Nat. Commun.* **2015**, 6 (1), 8379.
- (29) Xiao, D.; Liu, Y. J.; Yin, S.; Liu, J.; Ji, W.; Wang, B.; Luo, D.; Li, G.; Sun, X. W. Liquid-crystal-loaded chiral metasurfaces for reconfigurable multiband spin-selective light absorption. *Opt. Express* **2018**, 26 (19), 25305–25314.
- (30) Wu, Z.; Zheng, Y. Moiré chiral metamaterials. *Advanced Optical Materials* **2017**, *5* (16), 1700034.
- (31) Van Long, L.; Tung, N. H.; Giang, T. T.; Son, P. T.; Tung, N. T.; Tung, B. S.; Khuyen, B. X.; Lam, V. D. Rotary bi-layer ring-shaped metamaterials for reconfiguration absorbers. *Appl. Opt.* **2022**, *61* (30), 9078–9084.
- (32) Liu, S.; Ma, S.; Shao, R.; Zhang, L.; Yan, T.; Ma, Q.; Zhang, S.; Cui, T. J. Moiré metasurfaces for dynamic beamforming. *Science advances* **2022**, *8* (33), eabo1511.
- (33) Liu, Y.; Wu, Z.; Kollipara, P. S.; Montellano, R.; Sharma, K.; Zheng, Y. Label-free ultrasensitive detection of abnormal chiral metabolites in diabetes. *ACS Nano* **2021**, *15* (4), 6448–6456.
- (34) Wu, Z.; Kelp, G.; Yogeesh, M. N.; Li, W.; McNicholas, K. M.; Briggs, A.; Rajeeva, B. B.; Akinwande, D.; Bank, S. R.; Shvets, G.; et al. Dual-band moiré metasurface patches for multifunctional biomedical applications. *Nanoscale* **2016**, *8* (43), 18461–18468.
- (35) Yang, S. J.; Choi, M. Y.; Kim, C. J. Engineering Grain Boundaries in Two-Dimensional Electronic Materials. *Adv. Mater.* **2023**, 35, 2203425.
- (36) Lau, C. N.; Bockrath, M. W.; Mak, K. F.; Zhang, F. Reproducibility in the fabrication and physics of moiré materials. *Nature* **2022**, *602* (7895), 41–50.
- (37) Semaltianos, N.; Scott, K.; Wilson, E. Electron beam lithography of Moiré patterns. *Microelectronic engineering* **2001**, *56* (3–4), 233–239.
- (38) Lubin, S. M.; Zhou, W.; Hryn, A. J.; Huntington, M. D.; Odom, T. W. High-rotational symmetry lattices fabricated by moiré nanolithography. *Nano Lett.* **2012**, *12* (9), 4948–4952.
- (39) Ushkov, A.; Verrier, I.; Kampfe, T.; Jourlin, Y. Subwavelength diffraction gratings with macroscopic moiré patterns generated via laser interference lithography. *Opt. Express* **2020**, 28 (11), 16453–16468
- (40) Chen, K.; Rajeeva, B. B.; Wu, Z.; Rukavina, M.; Dao, T. D.; Ishii, S.; Aono, M.; Nagao, T.; Zheng, Y. Moiré nanosphere lithography. ACS Nano 2015, 9 (6), 6031–6040.
- (41) Chen, Z.; Xu, Z.; Zhang, M.; Zhou, Y.; Liu, M.; Patten, T.; Liu, G.-Y.; Li, H.; Zeng, X.; Tan, L. Two-dimensional crystallization of hexagonal bilayer with Moiré patterns. *J. Phys. Chem. B* **2012**, *116* (14), 4363–4369.
- (42) Carlson, A.; Bowen, A. M.; Huang, Y.; Nuzzo, R. G.; Rogers, J. A. Transfer printing techniques for materials assembly and micro/nanodevice fabrication. *Adv. Mater.* **2012**, *24* (39), 5284–5318.
- (43) Novoselov, K. S.; Geim, A. K.; Morozov, S. V.; Jiang, D.-e.; Zhang, Y.; Dubonos, S. V.; Grigorieva, I. V.; Firsov, A. A. Electric field effect in atomically thin carbon films. *science* **2004**, *306* (5696), 666–669.
- (44) Uwanno, T.; Hattori, Y.; Taniguchi, T.; Watanabe, K.; Nagashio, K. Fully dry PMMA transfer of graphene on h-BN using a heating/cooling system. 2D Materials 2015, 2 (4), No. 041002.
- (45) Van Ngoc, H.; Qian, Y.; Han, S. K.; Kang, D. J. PMMA-etching-free transfer of wafer-scale chemical vapor deposition two-dimensional atomic crystal by a water soluble polyvinyl alcohol polymer method. *Sci. Rep.* **2016**, *6* (1), 33096.

- (46) Kim, J.-W.; Yang, K.-Y.; Hong, S.-H.; Lee, H. Formation of Au nano-patterns on various substrates using simplified nano-transfer printing method. *Appl. Surf. Sci.* **2008**, 254 (17), 5607–5611.
- (47) Hassanin, H.; Mohammadkhani, A.; Jiang, K. Fabrication of hybrid nanostructured arrays using a PDMS/PDMS replication process. *Lab Chip* **2012**, *12* (20), 4160–4167.
- (48) Byun, I.; Coleman, A. W.; Kim, B. SAM meets MEMS: reliable fabrication of stable Au-patterns embedded in PDMS using dry peel-off process. *Microsystem technologies* **2014**, *20* (10), 1783–1789.
- (49) Wang, Q.; Han, W.; Wang, Y.; Lu, M.; Dong, L. Tape nanolithography: a rapid and simple method for fabricating flexible, wearable nanophotonic devices. *Microsystems & Nanoengineering* 2018, 4 (1), 31.
- (50) Yan, Z.; Pan, T.; Xue, M.; Chen, C.; Cui, Y.; Yao, G.; Huang, L.; Liao, F.; Jing, W.; Zhang, H.; et al. Thermal release transfer printing for stretchable conformal bioelectronics. *Advanced Science* **2017**, *4* (11), 1700251.
- (51) Zhang, J.; Wu, Y.; Li, Z.; Zhang, Y.; Peng, Y.; Chen, D.; Zhu, W.; Xu, S.; Zhang, C.; Hao, Y. High-performance acetone soluble tape transfer printing method for heterogeneous integration. *Sci. Rep.* **2019**, 9 (1), 15769.
- (52) Johnson, P. B.; Christy, R.-W. Optical constants of the noble metals. *Phys. Rev. B* **1972**, *6* (12), 4370.
- (53) Olmon, R. L.; Slovick, B.; Johnson, T. W.; Shelton, D.; Oh, S.-H.; Boreman, G. D.; Raschke, M. B. Optical dielectric function of gold. *Phys. Rev. B* **2012**, *86* (23), No. 235147.
- (54) Hagel, J.; Brem, S.; Malic, E. Electrical tuning of moiré excitons in MoSe2 bilayers. 2D Materials 2023, 10 (1), No. 014013.
- (55) Jeong, J. W.; Yang, S. R.; Hur, Y. H.; Kim, S. W.; Baek, K. M.; Yim, S.; Jang, H.-I.; Park, J. H.; Lee, S. Y.; Park, C.-O.; et al. High-resolution nanotransfer printing applicable to diverse surfaces via interface-targeted adhesion switching. *Nat. Commun.* **2014**, *5* (1), 5387.
- (56) Linghu, C.; Zhang, S.; Wang, C.; Song, J. Transfer printing techniques for flexible and stretchable inorganic electronics. *npj Flexible Electronics* **2018**, 2 (1), 26.
- (57) Ishikawa, F. N.; Chang, H.-k.; Ryu, K.; Chen, P.-c.; Badmaev, A.; Gomez De Arco, L.; Shen, G.; Zhou, C. Transparent electronics based on transfer printed aligned carbon nanotubes on rigid and flexible substrates. *ACS Nano* **2009**, *3* (1), 73–79.
- (58) Stelling, C.; Retsch, M. Nanomeshes at Liquid Interfaces: From Free-Standing Hole Arrays toward Metal—Insulator—Metal Architectures. *Advanced Materials Interfaces* **2018**, 5 (10), 1800154.

☐ Recommended by ACS

Meta-Atom Coupling Induced Chiral Hotspot in Silicon Nitride Staggered Nanorods Meta-Surface

Ziying Li, Chao Shen, et al.

MARCH 29, 2023

THE JOURNAL OF PHYSICAL CHEMISTRY LETTERS

READ 🗹

Chiral Lattice Resonances in 2.5-Dimensional Periodic Arrays with Achiral Unit Cells

Luis Cerdán, Aleiandro Manjavacas, et al.

MAY 10, 2023

ACS PHOTONICS

READ 🗹

Dynamic Control of Nonlinearly Generated Light Chirality with Nanostructured Graphene

Nikolaos Matthaiakakis, George Kakarantzas, et al.

APRIL 21, 2023

ACS APPLIED OPTICAL MATERIALS

READ 🗹

Extrinsic Chirality and Circular Dichroism at Visible Frequencies Enabled by Birefringent α -MoO $_3$ Nanoscale-Thick Films: Implications for Chiro-Optical Control

Emilija Petronijevic, Koray Aydin, et al.

APRIL 11, 2022

ACS APPLIED NANO MATERIALS

READ 🗹

Get More Suggestions >